RSC Advances

PAPER

Check for updates

Cr₂O₃ nanosheet/carbon cloth anode with strong interaction and fast charge transfer for pseudocapacitive energy storage in lithium-ion batteries†

Donglei Guo,[a] Mengke Yang,[a] Lilei Zhang,[a] Yicong Li,[a] Jinxiang Wang,[a] Guilong Liu, [ID][a] Naiteng Wu, [ID][ac] Jang-Kyo Kim [ID]*[b] and Xianming Liu [ID]*[a]

Flexible lithium-ion batteries have attracted considerable interest for next-generation bendable, implantable and wearable electronics devices. Here, we have successfully grown Cr₂O₃ nanosheets on carbon cloth (CC) as freestanding anodes for Li-ion batteries (LIBs). Density functional theory (DFT) calculations verify an optimal structure of two-dimensional Cr₂O₃ nanosheets on the carbon fiber surface and a strong interaction between the O edges of Cr₂O₃ and the carbon. The interconnected Cr₂O₃ nanosheets with a large surface area enable fast charge transfer by efficient contact with electrolyte while the flexible CC substrate accommodates the volume change during cycles, leading to excellent rate capability and cyclic stability through psuedocapacitance-dominant energy storage. Full cells are assembled using the Cr₂O₃-CC anode and a LiFePO₄ cathode, which deliver excellent capacity retention and rate capability. The fully-charged cell is demonstrated to power a red light-emitting diode (LED), verifying the potential of Cr₂O₃-CC as a promising anode material for LIBs.

Introduction

The recent rise in flexible and bendable electronics such as rollup displays, smart electronics and wearable devices, has prompted the development of flexible lithium-ion batteries (LIBs) due to their high energy density, long cycle life, high rate capacity and safety.[1–3] The key challenge to realizing high performance, flexible LIBs is to design and fabricate reliable flexible electrodes with high-rate capability, cyclic stability and mechanical robustness and flexibility.[4–6] An effective strategy to prepare flexible electrodes for flexible LIBs is by growing or coating electrochemically active materials on a flexible, conductive membrane substrate without conductive additives or binders.[7–9] In order to meet the required high-performance flexible LIBs in practical applications, the selection and design of flexible membrane substrates with good mechanical properties and excellent electrical conductivities are of utmost

importance. Flexible carbon cloth (CC) prepared from carbon fibers is considered as an excellent choice possessing a high electrical conductivity, a unique porous structure, high mechanical integrity and good corrosion resistance, and has been increasingly used in various energy storage devices.[10–12]

Among the various proposed high-capacity anode materials for LIBs, such as carbonaceous materials,[13,14] simple substances,[15,16] alloy materials,[17,18] transitional-metal oxides (TMOs)[19,20] and metal sulfides,[21,22] TMOs have high theoretical capacities, low costs, simple preparation methods and environmental benignity.[23,24] Among them, Cr₂O₃ is considered a promising anode material with a high theoretical capacity of 1058 mA h g⁻¹ and a relative low electromotive force of 1.085 V vs. Li⁺/Li.[25,26] The Li-ion storage mechanism of Cr₂O₃ can be represented by the following conversion reaction: Cr₂O₃ + 6Li⁺ ↔ 2 Cr + 3 Li₂O. As in other TMOs, however, bulk Cr₂O₃ materials usually suffer from poor cyclic stability and rate capacity due to the significant volume change and the aggregation of pulverized or nanosized particles, hindering their practical applications. These issues have been resolved by introducing conductive carbon substrates to enhance the electronic conductivity and accommodate the volume changes occurring during the charge/discharge cycles.[26–31] For example, the mesoporous carbon–Cr₂O₃ composite exhibited an initial reversible capacity of 710 mA h g⁻¹ and good cyclic stability.[26] Ultrasmall Cr₂O₃ nanoparticles were incorporated in a carbon nanocapsule configuration by a surfactant-free solvothermal

[a] Key Laboratory of Function-Oriented Porous Materials, College of Chemistry and Chemical Engineering, Luoyang Normal University, Luoyang, 471934, P. R. China. E-mail: myclxm@163.com

[b] Department of Mechanical and Aerospace Engineering, Hong Kong University of Science and Technology, Clear Water Bay, Kowloon, Hong Kong, P. R. China. E-mail: mejkkim@ust.hk

[c] College of Materials and Chemical Engineering, China Three Gorges University, Yichang, 443002, P. R. China

route with renewable furfural as the carbon source, achieving 568 mA h g^{-1} after more than 200 cycles at a current density of 100 mA g^{-1}.[27] Cr_2O_3/carbon nanosheet composites were synthesized by a solution combustion method, which exhibited an initial capacity of 1680 mA h g^{-1}.[28] Although the electrochemical performance of the Cr_2O_3 anodes greatly improved, there remain critical issues that need to be resolved. For example, the carbon content in the composite electrode was typically more than 25 wt%, which is excessive. Moreover, conventional Cr_2O_3-based electrodes generally required substantial amounts of conductive additives and binders to improve their electronic conductivity and mechanical integrity. However, the additives and binders make no or a very few capacity contribution to the electrodes, while the weak binding force between the active materials and the current collector inevitably leads to the detachment of active materials from the current collector, resulting in capacity fading.[32] A higher permeability and more active sites were reported with improved electrochemical performance when the TMOs with a large surface area in the 3D architecture were assembled by nanostructured building blocks.[33–35] Hence, constructing binder-free Cr_2O_3 anodes with a 3D architecture is highly desirable.

With the above background, we herein report the synthesis of 2D Cr_2O_3 nanosheets grown on carbon cloth (Cr_2O_3-CC) by a facile hydrothermal method and subsequent thermal treatment for lithium-ion batteries. The 3D architecture of Cr_2O_3 nanosheets not only prevented self-aggregation of electrode materials to create large surface areas for efficient charge transfer through the electrolyte, but also buffered the volume expansion and mitigated mechanical stresses of the electrode during the charge/discharge cycles, improving the structural integrity of the electrode. The Cr_2O_3-CC was used as a binder-free anode for LIBs, which delivered a high reversible capacity of 414.2 mA h g^{-1} at a current density of 2 A g^{-1} and 916.6 mA h g^{-1} at a current density of 0.1 A g^{-1} after 200 cycles. Moreover, a full cell was assembled by coupling with a commercial $LiFePO_4$ cathode, which exhibited excellent cyclic performance and superior rate capacity, proving potential for practical application.

Experimental section

Synthesis of Cr_2O_3-CC and Cr_2O_3 nanoparticles

All chemicals used in this work were of analytical grade without further purification. Carbon cloth (CC) was pretreated by refluxing in concentrated HNO_3 at 100 °C for 2 h to remove impurities, and washed with deionized (DI) water and ethanol several times for further use. In a typical procedure, 0.8 g chromium nitrate ($Cr(NO_3)_3 \cdot 9H_2O$) and 0.08 g urea (CH_4N_2O) were dissolved in 80 mL distilled water under continuous stirring, then the solution was stirred for 1 h to form a uniform and dark blue solution. Subsequently, the pretreated CC was immersed in the solution, which was transferred into a 100 mL Teflon-lined stainless steel autoclave and kept at 180 °C for 12 h. After the autoclave was cooled down to room temperature, the CC coated with CrOOH nanosheets (CrOOH-CC) was removed and washed with DI water and ethanol. The as-prepared

CrOOH-CC was calcined at 500 °C for 3 h in air at a heating rate of 2 °C min^{-1} to convert to CC coated with Cr_2O_3 nanosheets (Cr_2O_3-CC). The mass loading of Cr_2O_3 in Cr_2O_3-CC was calculated to be 7.94 wt% based on the weight difference of CC before and after loading Cr_2O_3. In addition, by controlling the time of hydrothermal we also have prepared another mass loading of Cr_2O_3-CC with Cr_2O_3 loadings of 6.7 wt% (6 h) and 9.97 wt% (18 h). For comparison, Cr_2O_3 nanoparticles (NPs) were also prepared in a manner similar to that of Cr_2O_3-CC, except for the absence of CC in the synthesis process.

Characterizations

The composition and phase purity of the samples were analyzed by powder X-ray diffraction (XRD) with monochromatized Cu Kα incident radiation on a Shimadzu XRD-6000 operated at 40 kV voltage and 40 mA current. The morphology of the products were characterized by a field-emission scanning electron microscope (FESEM, Sigma 500) and a H-8100 transmission electron microscope (TEM) operating at 200 kV accelerating voltage. Energy-dispersive X-ray (EDX) element maps were taken on a Sigma 500 FESEM unit. Raman spectra were collected on an Invia Raman spectrometer with the excitation laser wavelength of 633 nm. X-ray photoelectron spectra (XPS) were recorded on an ESCALAB 250 spectrometer (Perkin-Elmer).

Electrochemical measurements

All half-cell tests were performed using CR2032 coin cells assembled in an argon-filled glove box with moisture and oxygen contents below 0.1 ppm. The flexible, freestanding Cr_2O_3-CC was directly cut into disks of ~1.13 cm^2 in area as the working electrode and a lithium metal foil as the counter electrode. For the preparation of Cr_2O_3 NP electrodes, the active material, conductive carbon black and polyvinylidene fluoride (PVDF) binder were mixed at a mass ratio of 80 : 10 : 10 and ground using a mortar. N-Methyl-2-pyrrolidone (NMP) solvent was added to prepare homogeneous slurry. The slurry was uniformly pasted on Cu foil current collector and dried in a vacuum oven at 80 °C for 12 h and then 120 °C for another 12 h. The charge/discharge profiles of the electrodes were determined in the potential range of 0.01–3 V at different current rates. Cyclic voltammetry (CV) curves were determined at different scanning rates from 0.1 to 1.0 mV s^{-1} and electrochemical impedance spectra (EIS) were obtained in the frequency range from 100 000 to 0.05 Hz at an AC amplitude of 5 mV on a Parstat 4000 + workstation (Princeton Applied Research).

The full cells were prepared using the commercial $LiFePO_4$ powder as the cathode and the Cr_2O_3-CC film as the anode. The $LiFePO_4$ cathode film was fabricated by coating a mixture of $LiFePO_4$, carbon black and PVDF binder at a weight ratio of 80 : 10 : 10 onto the Al current collector and drying in a vacuum oven at 80 °C for 12 h followed by 120 °C for another 12 h. The mass loadings of the Cr_2O_3-CC anode and the $LiFePO_4$ cathode were matched based on their capacities, and there was a slight excess capacity for the cathode compared with the anode. The full cells, Cr_2O_3-CC//$LiFePO_4$, were assembled in an argon-filled

glove box, which were cycled in the voltage range of 1–3.7 V. As for aluminium laminated soft-packed cells, the Cr_2O_3-CC film was cut into 2 cm × 3 cm rectangle slice for rectangle cell anode. This work appears to be the first report on electrochemical performance of full cells prepared from Cr_2O_3 anodes.

Density functional theory (DFT) calculations

The detailed interaction mechanisms taking place between the Cr_2O_3 nanosheets and the carbon fibers were studied by density functional theory (DFT) calculations using the Vienna *ab initio* simulation package (VASP).[36,37] All calculations were performed using general gradient approximations (GGA) and periodic boundary conditions to model the exchange and correlation interactions.[36] Perdew–Burke–Ernzerhof (PBE) functionals, projector augmented wave (PAW) pseudopotentials and the DFT-D2 correction were applied to represent the van der Waals interactions.[37–39] A plane wave basis set with an energy cut-off of 500 eV was employed in the calculation. The *k*-point meshes were sampled based on the Monkhorst–Pack method. DFT calculations were performed on the experimental crystalline structure of Cr_2O_3. The formation energies were calculated on slab models consisting of Cr_2O_3 and graphene layers, while the nudged elastic bands (NEBs) were calculated on a bulk Cr_2O_3 model. All the models were sampled on a Monkhorst–Pack 2 × 2 × 1 meshes and the self-consistence of electrons was converged to 10^{-6} eV.

Results and discussion

The preparation procedure of Cr_2O_3-CC is schematically illustrated in Fig. 1, which involved two steps. First, CrOOH nanosheets were *in situ* grown on CC by a facile hydrothermal method (Fig. S1a†). Then, the Cr_2O_3-CC composite was obtained by annealing at 500 °C for 3 h in air. The XRD patterns given in Fig. 2a indicate that all diffraction peaks of Cr_2O_3-CC and Cr_2O_3 NPs can be assigned to the rhombohedral crystal structure (JCPDS card no. 84-0312). The peaks at 26.2° and 43.5° can be indexed to carbon arising from CC (Fig.S1b†). The Raman spectra shown in Fig. 2b exhibit two distinct peaks at ∼1340 and ∼1600 cm^{-1}, which can be assigned to the D- and G-bands of CC, representing disordered phonon mode and graphitic structure, respectively. The bands below 400 cm^{-1} can be assigned to the external modes of Cr_2O_3 (shown in the inset of Fig. 2b), while the disappearance or weakening of the Raman fingerprint characteristic of Cr_2O_3-CC was caused by screening effects of CC. The XPS survey spectrum (Fig. 2c) discloses that Cr_2O_3-CC consisted of Cr, O and C elements. The high-resolution Cr 2p spectrum (Fig. 2d) shows two peaks at 586.5 and 576.7 eV which could be ascribed to Cr $2p_{1/2}$ and Cr $2p_{3/2}$, respectively.[28] The high-resolution O 1s spectrum (Fig. 2e) has two peak at 530.3 and 531.8 eV corresponding to the O–Cr and O═C bonds, respectively, whereas the C 1s spectrum (Fig. 2f) displays two peaks at 284.8 and 288.5 eV that can be ascribed to the C–C and O═C–O groups, respectively.

The digital photographs, FESEM and TEM images of Cr_2O_3-CC are given in Fig. 3 presenting its morphological and
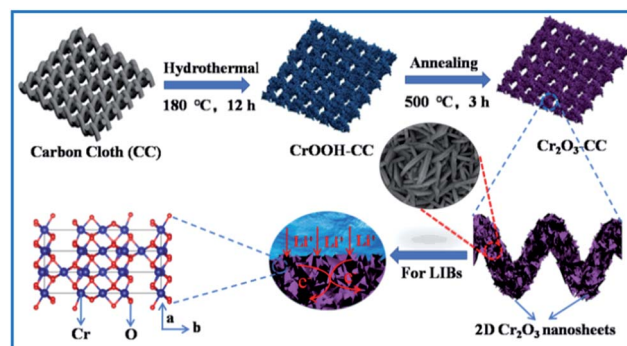

Fig. 1 Schematic diagram of the preparation procedure of Cr_2O_3-CC with 2D Cr_2O_3 nanosheets grown on CC.

structural features. The Cr_2O_3-CC composite paper was flexible, mechanically robust and could be bent into arbitrary shapes (Fig. 3a and b). Moreover, it could be cut into disks of ∼1.13 cm^2, which were used as freestanding anodes without adding binder or carbon additives (Fig. 3c). The Cr_2O_3-CC composite consisted of interconnected 2D Cr_2O_3 nanosheets grown on carbon fibers (Fig. 3d and e). The morphologies of Cr_2O_3-CC were essentially similar to the intermediate product, CrOOH-CC, obtained before annealing (Fig. S2 and S3a–c†), signifying that the structure of Cr_2O_3-CC remained unaltered even after annealing. The EDX measurement of Cr_2O_3-CC confirmed the co-existence of Cr, O and C elements (Fig. S4†), which were
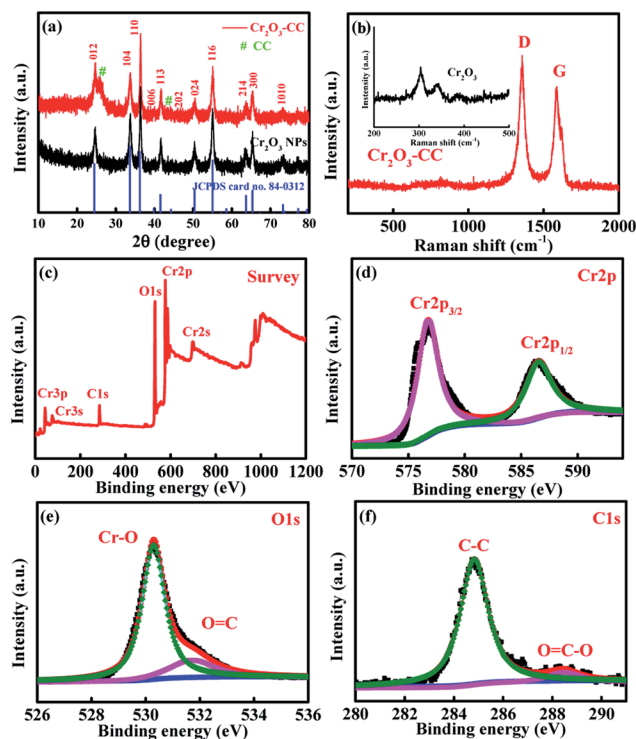

Fig. 2 (a) XRD patterns of Cr_2O_3-CC and Cr_2O_3 NPs; (b) Raman spectra of Cr_2O_3-CC and Cr_2O_3 NPs (in inset); (c–f) XPS spectra of Cr_2O_3-CC: (c) survey spectrum, and deconvoluted spectra of (d) Cr 2p, (e) O 1s and (f) C 1s.
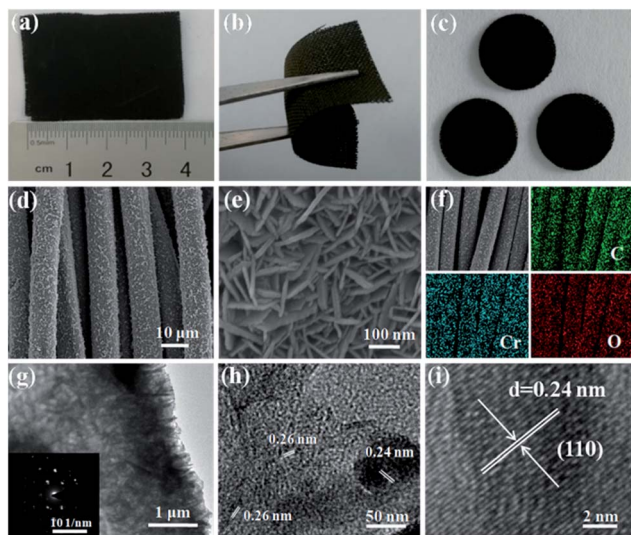
Fig. 3 (a–c) Digital photographs of flexible Cr_2O_3-CC which is cut into disks of 1.13 cm^2 in area as the working electrode without binder or carbon additives; (d and e) FESEM images of Cr_2O_3-CC, (f) element maps of Cr_2O_3-CC, and (g–i) HRTEM images of Cr_2O_3-CC, corresponding SEAD pattern in inset of (g).

distributed uniformly along the whole carbon fiber surface, as confirmed by the elemental maps (Fig. 3f). An interesting architecture was uncovered by the HRTEM images (Fig. 3g and h) where the 2D Cr_2O_3 nanosheets were closely interconnected on the carbon fiber substrate. The Cr_2O_3-CC composite with a large surface area, once used as the anode, not only allowed fast charge transfer through the short diffusion pathways of Cr_2O_3 nanosheets, but also accommodated the volume expansion of Cr_2O_3 during the charge/discharge cycles by the CC substrate. The selected-area electron diffraction (SAED) pattern (in inset of Fig. 3g) revealed a polycrystalline nature of Cr_2O_3-CC. The marked lattice fringes with d-spacings of 0.24 and 0.26 nm correspond to the (104) and (110) planes of Cr_2O_3-CC (Fig. 3h and i).

The electrochemical performance of the Cr_2O_3-CC and Cr_2O_3 NP anodes for LIBs is shown in Fig. 4. The discharge/charge voltage profiles (Fig. 4a) present the discharge and charge capacities of 1547.8 and 1310 mA h g^{-1}, respectively, upon the first cycle of the Cr_2O_3-CC electrode along with an initial coulombic efficiency (CE) of 84.7%. The irreversible capacity loss in the first cycle can be attributed to the inevitable decomposition of electrolyte and the formation of solid electrolyte interface (SEI) on the electrode surface.[40,41] Obviously, the Cr_2O_3-CC electrode exhibited much stabler cyclic stability than the Cr_2O_3 NP counterpart, with a high discharge capacity of 917.3 mA h g^{-1} retained after 200 cycles at 0.1 A g^{-1} for the former (Fig. 4b). In addition, an almost 100% CE was maintained in the second cycle and on wards of the Cr_2O_3-CC electrode, indicating its high reversibility. The cyclic performances of Cr_2O_3-CC with different mass loadings of Cr_2O_3 were also tested (Fig. S5†), indicating the Cr_2O_3-CC (7.94 wt%) shows the best performance. The relative cyclic performance of CC was poor with very low specific capacities (Fig. S6a†), confirming its

almost negligible capacity contribution to the Cr_2O_3-CC electrode. The Cr_2O_3-CC electrode delivered high capacities of 1210, 1092, 914.4, 752.4, 540 and 414.2 mA h g^{-1} at 0.1, 0.2, 0.4, 0.8, 1 and 2 A g^{-1}, respectively, which were 300–500 mA h g^{-1} higher than the corresponding values of the Cr_2O_3 NP counterpart, as shown in Fig. 4c. When the rate was reverted to 0.1 A g^{-1}, the capacity of Cr_2O_3-CC recovered to 1005 mA h g^{-1}, indicative of remarkable electrochemical reversibility and robustness of the electrode. Fig. 4d shows the long-term cyclic stability of the Cr_2O_3-CC electrode at 0.8 A g^{-1}, which was tested without pre-activation. Remarkably, it exhibited outstanding cyclic performance with a high discharge capacity of 397 mA h g^{-1} after 400 cycles at 0.8 A g^{-1}. It is worth noting that these values are better than or on par with the state-of-the-art results reported on similar Cr_2O_3 anodes (see details in Table 1). The inset Fig. 4d presents a digital and FESEM images taken of the Cr_2O_3-CC electrode after 400 cycles. It is clearly seen that the Cr_2O_3 nanosheets remained largely intact on the carbon fiber substrate without any signs of fracture or decomposition, signifying a robust and durable structure in the corrosive chemical environment of the electrolyte. The robust and flexible carbon fibers in CC functioned as buffer to accommodate volume changes while offering a large surface area for electrolyte. Fig. 4e shows the EIS spectra of the Cr_2O_3-CC and Cr_2O_3 NP electrodes. The high frequency intercept at the Z′ axis corresponds to the ohmic resistance (R_s), which represents the
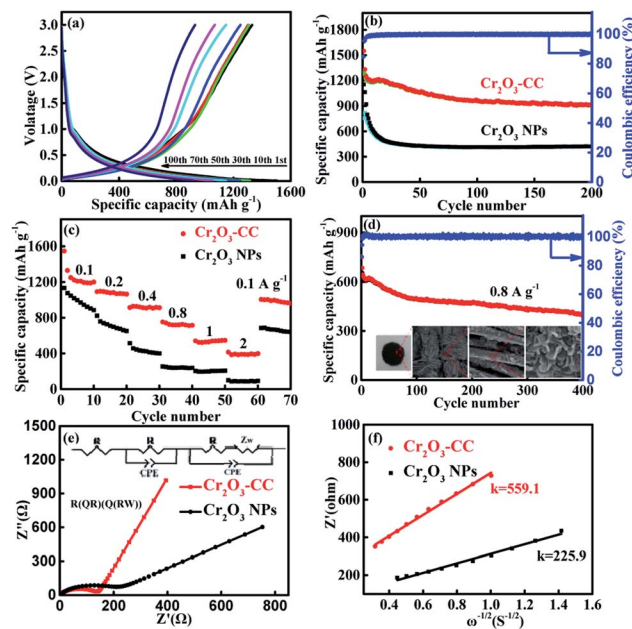

Fig. 4 (a) Discharge/charge voltage profiles of Cr_2O_3-CC at a current density of 0.1 A g^{-1}; (b) cyclic performance of Cr_2O_3-CC and Cr_2O_3 NPs at a current density of 0.1 A g^{-1} and the corresponding CE of Cr_2O_3-CC; (c) rate performance of Cr_2O_3-CC and Cr_2O_3 NPs at current densities ranging from 0.1 to 2 A g^{-1}; (d) long-term cyclic performance of Cr_2O_3-CC at a current density of 0.8 A g^{-1}, and digital and FESEM images of Cr_2O_3-CC electrode after 400 cycles in inset; (e) EIS spectra of Cr_2O_3-CC and Cr_2O_3 NPs, and (f) the corresponding linear fits of the slopes in the low frequency region after 100 cycles at 0.1 A g^{-1}.

Table 1 Comparison of the electrochemical performance of this work with previously reported Cr_2O_3-based electrodes

Cr_2O_3-based electrodes	Synthesis method	Current density (mA g^{-1})/rate	Cycle number	Specific capacity (mA h g^{-1})	Ref.
Cr_2O_3 sheet	Solution combustion	100	55	480	25
M-C-Cr_2O_3	Template method	50	80	639	26
Cr_2O_3-NPs@NC	Hydrothermal method	100	203	568	27
Cr_2O_3/C	Solution combustion	100	55	710	28
Cr_2O_3–C	Non-sacrificial template	200	35	600	29
Cr_2O_3-CNT$_{(0.08\%)}$	Chemical co-precipitation method	100	200	995.3	30
Cr_2O_3/carbon	Sol–gel approach	100	150	465.5	31
Cr_2O_3/C	Ballmilling	100	20	650	46
Cr_2O_3/FLG/Ni	Pulsed laser deposited	100	50	543	47
graphene/Cr_2O_3	Hydrothermal method	0.1C	100	580	48
Cr_2O_3/NC	Bio-template method	100	100	640	49
		1000	50	360	
Graphene-Cr_2O_3	Hydrothermal method	200	50	850	50
C–Cr_2O_3	Vacuum assisted impregnation	0.1C	100	540	51
Cr_2O_3/C nanofiber	Electrospinning	100	100	527	52
Cr_2O_3@C@G	Spray drying	100	120	648	53
Cr_2O_3/C	Ballmilling	100	50	530	54
Cr_2O_3-GICs	Intercalation transformation	100	1000	520	55
Our work (Cr_2O_3-CC)	Hydrothermal method	100	200	916.6	
		800	400	414.2	

resistance of the electrolyte solution, and the semicircle in the mid-frequency range corresponds to the charge transfer resistance (R_{ct}). The inclined line in the low frequency range represents the Warburg impedance (Z_w), which is associated with Li$^+$ diffusion. The EIS spectra were fitted with the circuit model given in inset of Fig. 4e and the impedance parameters thereby determined are summarized in Table S1.† The R_{ct} value was much smaller for Cr_2O_3-CC than for Cr_2O_3 NPs, *i.e.* 140 *vs.* 217 Ω, indicating a faster charge transfer for the former electrode. Z_w is a measure of lithium diffusion within the electrode and thus a higher slope with a lower Z_w value of Cr_2O_3-CC meant

better lithium diffusion than Cr_2O_3 NPs.[42] The lithium ion diffusion coefficient, D_{Li^+}, is given by eqn (1):[43–45]

$$D_{Li^+} = [RT/\sqrt{2}(An^2F^2\sigma C)]^2 \qquad (1)$$

where R is the gas constant, T is the absolute temperature, A is the surface area of the electrode, n is the number of electrons per molecule during oxidation, F is the Faraday's constant, σ is Warburg factor obtained from the slope of Z' *vs.* $\omega^{-1/2}$ in the low frequency region (Fig. 4f), and C is the molar concentration of Li ions in the electrode. According to eqn (1), D_{Li^+} is proportional to σ^{-2} while all other parameters are constant for a given electrode material. It follows then that the D_{Li^+} value of the Cr_2O_3-CC electrode was approximately 9 times higher than that of the Cr_2O_3 NP electrode, see Table S1.†
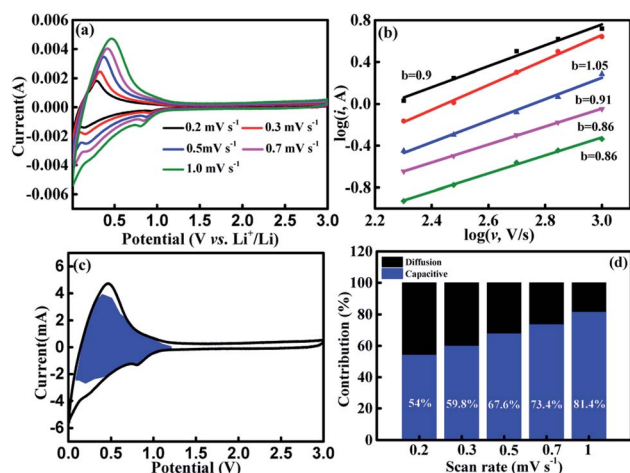

Fig. 5 Kinetics analyses of Cr_2O_3-CC: (a) CV curves obtained at different scan rates; (b) log(i) *vs.* log(v) plots at different voltages; (c) pseudocapacitive contribution (blue region) to charge storage at 1 mV s^{-1}; (d) the ratio of pseudocapacitive and diffusion-controlled contributions at different scan rates.
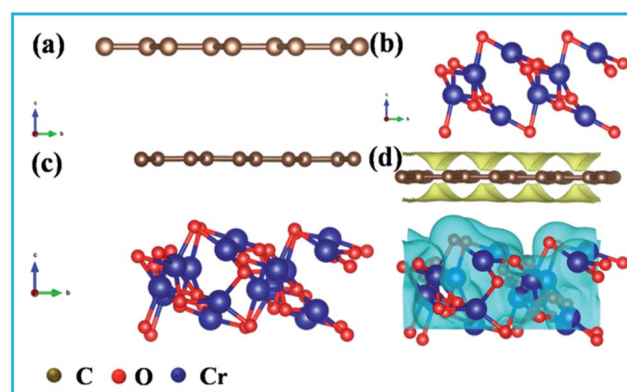

Fig. 6 Optimal structures of (a) carbon, (b) Cr_2O_3 and (c) Cr_2O_3-CC used in density functional theory calculations; (d) Electron density difference of Cr_2O_3 nanosheets vertically grown on carbon surface.

To explain the excellent rate performance of Cr_2O_3-CC, its kinetics was analyzed and the sources of capacity were probed, as shown in Fig. 5. The CV curves displayed essentially a similar shape and a broad peak profile for all scan rates between 0.2 to 1.0 mV s^{-1} (Fig. 5a) and for the first five cycles at 0.1 mV s^{-1} (Fig. S7†). In general, both the intercalation and capacitive reactions contribute to capacities of the electrodes at a high current density.[45,56] The $\log(i)$ *vs.* $\log(\nu)$ plots of the Cr_2O_3-CC electrode are presented in Fig. 5b at different voltages, where the slope of the fitted line is denoted by b. When the b value approaches 1, the electrochemical system is controlled mainly by the pseudocapacitive effect, but when the b value is close to 0.5, the ionic diffusion process dominates. Here, the b values are seen higher than 0.8, signifying a high pseudocapacitive contribution.[57] The individual contributions from both the pseudocapacitive ($k_1 \nu$) and diffusion-controlled responses ($k_2 \nu^{1/2}$) were quantitatively analyzed based on the exponential relationship with scan rate:[56–58]

$$i = k_1 \nu^{1/2} + k_2 \nu^{1/2} \qquad (2)$$

where k_1, k_2 are the constants, and ν is the scan rate. By calculating the k_1 and k_2 values at different voltages (Fig. S8†), the ratios of the pseudocapacitive to diffusion-controlled contributions were determined, as shown in Fig. 5c. It is obvious that the pseudocapacitive contribution was dominant for the Cr_2O_3-CC electrode, which increased gradually from 54% at 0.2 mV s^{-1} to ~81.4% at 1 mV s^{-1} with increasing scan rate (Fig. 5d and S9). It is proposed previously the surface-driven pseudocapacitive contribution played a major role for charge storage in the unique nanosheet structures of SnS_2, Sb_2S_3 and MoO_2 with large surface areas for efficient reaction with electrolyte.[58–60]

To explore the mechanisms behind the growth of Cr_2O_3 on carbon fibers, the DFT calculations were performed and the formation energy, E_f, of horizontally-stacked Cr_2O_3-CC was obtained according to eqn (3), where $E_{Cr2O3-CC}$, E_{Cr2O3} and E_{CC} are the total DFT energies of Cr_2O_3-CC, Cr_2O_3 and CC, respectively:

$$E_f = E_{Cr_2O_3\text{-}CC} - E_{Cr_2O_3} - E_{CC} \qquad (3)$$

The optimized structures of CC, Cr_2O_3 and Cr_2O_3-CC are shown in Fig. 6a–c. A negative formation energy, $E_f = -0.52$ eV, was obtained for Cr_2O_3-CC, signifying thermodynamically favorable growth of Cr_2O_3 nanosheets on carbon fibers (Fig. 6d) during the annealing process.

To demonstrate practical applications of Cr_2O_3-CC electrodes with superior half-cell electrochemical performance, full cells were assembled using the Cr_2O_3-CC anode and a commercial $LiFePO_4$ (LFP) cathode, as schematically shown in Fig. 7b. Fig. 7a shows the XRD pattern of LFP@C with its FESEM image in inset, presenting spherical nanoparticles of ~300 nm in diameter. Before the full cell was assembled, the Cr_2O_3-CC anode was pre-lithiated by direct contact with Li foil. In designing the full-cell battery, it is of paramount importance to optimize the loadings of cathode and anode to achieve the best electrochemical performance.[61,62] Fig. 7c shows the voltage profiles of the full battery for voltages ranging 1–3.7 V at 1C for 1, 10, 30, 50 and 100 cycles. The initial discharge capacity was 152.4 m Ah g^{-1} calculated based on the cathode mass (1C = 170 mA g^{-1} *vs.* LFP), with an initial CE as high as 95.3%. The Cr_2O_3-CC//LFP@C full cell delivered excellent cyclic stability with a remaining discharge capacity of 140.6 mA h g^{-1} after 100 cycles (Fig. 7d), as well as superior rate performance (Fig. 7e). Specifically, the average capacities of the full cell were 150.6,
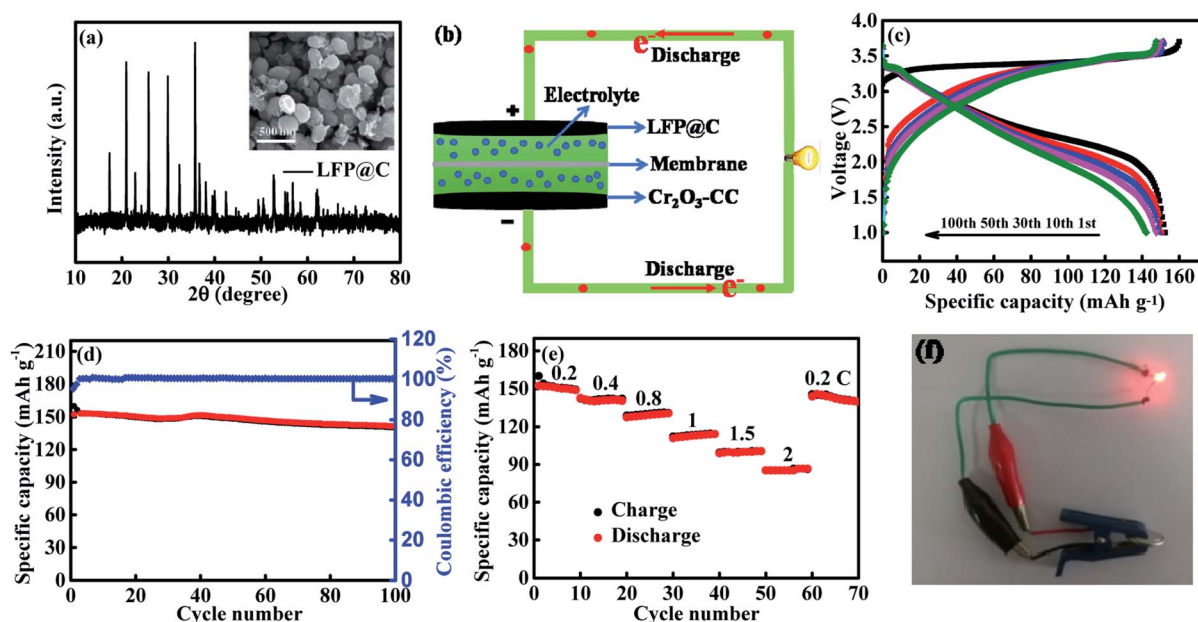

Fig. 7 (a) XRD pattern of commercial LFP@C and its FESEM image in inset; (b) schematic illustration of a full cell consisting of Cr_2O_3-CC anode and LFP@C cathode; (c) voltage-capacity profiles of Cr_2O_3-CC//LFP@C full cell in the voltage range 1–3.7 V at 0.2 C; (d) cyclic performance and corresponding coulombic efficiency of Cr_2O_3-CC//LFP@C full cell at 0.2 C; (e) rate performance of Cr_2O_3-CC//LFP@C full cell at different rates; (f) LED bulb lit by the assembled full cell.

141, 129.1, 112.8, 99.9 and 85.7 mA h g^{-1} at 0.2, 0.4, 0.8, 1, 1.5, and 2 C, respectively. The long-term cyclic stability and the corresponding CE of the Cr$_2$O$_3$-CC//LFP@C full cell is shown in Fig. S10.† It is seen that the full cell exhibited 88.8% capacity retention for over 500 cycles at 1C. A CE of almost 100%, a crucial property for full cells, was maintained throughout the whole cycles after the initial value of 92.4%, verifying excellent reversibility of charge and discharge cycles. The real-world application of the full cell was also demonstrated to power a red light-emitting diode (LED with 2 V and 10 mW) bulb, as shown in Fig. 7f, which partly confirm the potential of Cr$_2$O$_3$-CC as the promising anode material for next-generation LIBs. Morever, when the flexible full cell was assembled using the commercial LiFePO$_4$ powders as cathode as shown in Fig. S11,† a red light-emitting diode (LED) can be easily lighted at the bended state. The result confirms the potentiality of Cr$_2$O$_3$-CC as a anode material for flexible LIBs

Conclusions

In summary, we employed a simple hydrothermal method followed by thermal treatment to grow for the first time 2D Cr$_2$O$_3$ nanosheets on CC. The Cr$_2$O$_3$-CC composite was directly used as the freestanding anode without binder or conductive additives, which exhibited excellent lithium storage performance in terms of specific capacity, cyclic stability and rate capability. The interconnected Cr$_2$O$_3$ nanosheets on the CC substrate enabled fast charge transfer due to the short pathways of Cr$_2$O$_3$, while the conductive and flexible CC accommodated the volume expansion of Cr$_2$O$_3$ during the charge/discharge cycles. Moreover, the robust and durable structure with a large surface area gave rise to a high pseudocapacitance of Cr$_2$O$_3$-CC. Additionally, the full cell assembled with the Cr$_2$O$_3$-CC anode and a LiFePO$_4$@C cathode manifested excellent capacity retention and rate capability. The design concept developed in this work is universal to all types of rechargeable batteries and can be readily extended to other electrode materials requiring superior capacities and rate performance.

Conflicts of interest

There are no conflicts to declare.

Acknowledgements

Notes and references

1 M. S. Balogun, H. Yang, Y. Luo, W. T. Qiu, Y. C. Huang, Z. Q. Liu and Y. X. Tong, *Energy Environ. Sci.*, 2018, **11**, 1859–1869.

2 C. Chen, Y. Zhang, Y. Li, Y. Kuang, J. Song, W. Luo, Y. Wang, Y. Yao, G. Pastel and J. Xie, *Adv. Energy Mater.*, 2017, **7**, 1700595.

3 X. F. Wang, X. H. Lu, B. Liu, D. Chen, Y. X. Tong and G. Z. Shen, *Adv. Mater.*, 2014, **26**, 4763–4782.

4 G. M. Zhou, F. Li and H. M. Cheng, *Energy Environ. Sci.*, 2014, **7**, 1307–1338.

5 Z. Gao, N. Song, Y. Zhang and X. Li, *Nano Lett.*, 2015, **15**, 8194–8203.

6 J. Cui, S. Yao, W. G. Chong, J. Wu, M. Ihsan-Ul-Haq, M. Zhao, Y. Wang and J. K. Kim, *Chem. Mater.*, 2019, **31**, 4113–4123.

7 R. J. Zou, Z. Y. Zhang, M. F. Yuen, M. L. Sun, J. Q. Hu, C. S. Lee and W. J. Zhang, *NPG Asia Mater.*, 2015, **7**, 195–212.

8 Z. X. Liu, H. F. Li, M. S. Zhu, Y. Huang, Z. J. Tang, Z. X. Pei, Z. F. Wang, Z. C. Shi, J. Liu, Y. Huang and C. Y. Zhi, *Nano Energy*, 2018, **44**, 164–173.

9 Z. N. Deng, H. Jiang, Y. J. Hu, Y. Liu, L. Zhang, H. L. Liu and C. Z. Li, *Adv. Mater.*, 2017, **29**, 1603020.

10 D. L. Guo, J. W. Qin, Z. G. Yin, J. M. Bai, Y. K. Sun and M. H. Cao, *Nano Energy*, 2018, **45**, 136–147.

11 J. Q. Tian, Q. Liu, A. M. Asiri and X. P. Sun, *J. Am. Chem. Soc.*, 2014, **136**, 7587–7590.

12 G. H. Zhang, S. C. Hou, H. Zhang, W. Zeng, F. L. Yan, C. C. Li and H. G. Duan, *Adv. Energy Mater.*, 2015, **27**, 2400–2405.

13 W. H. Li, M. W. Li, K. R. Adair, X. L. Sum and Y. Yu, *J. Mater. Chem. A*, 2017, **5**, 13882–13906.

14 X. Ao, H. Y. Sun, C. D. Wang, J. G. Li, Y. J. Ruan, B. Z. Li, Q. H. Wu, Y. Li, J. J. Jiang, Y. G. Yang and L. Q. Mai, *Carbon*, 2018, **130**, 599–606.

15 Q. B. Zhang, H. X. Chen, L. L. Luo, B. T. Zhao, H. Luo, X. Han, J. W. Wang, C. M. Wang, Y. Yang, T. Zhu and M. L. Liu, *Energy Environ. Sci.*, 2018, **11**, 669–681.

16 S. Liu, J. K. Feng, X. F. Bian, Y. T. Qian, J. Liu and H. Xu, *Nano Energy*, 2015, **13**, 651–657.

17 Y. B. Zhao and A. Manthiram, *Chem. Mater.*, 2015, **27**, 3096–3101.

18 W. Xiao, J. Zhou, L. Yu, D. H. Wang and X. W. Lou, *Angew. Chem., Int. Ed.*, 2016, **55**, 7427–7431.

19 G. L. Liu, H. H. Wu, Q. Q. Meng, T. Zhang, D. Sun, X. Y. Jin, D. L. Guo, N. T. Wu, X. M. Liu and J. K. Kim, *Nanoscale Horiz.*, 2019, DOI: 10.1039/C9NH00402E.

20 N. T. Wu, W. Z. Du, X. Gao, L. Zhao, G. L. Liu, X. M. Liu, H. Wu and Y. B. He, *Nanoscale*, 2018, **10**, 11460–11466.

21 L. Z. Zhao, H. H. Wu, C. H. Yang, Q. B. Zhang, G. M. Zhong, Z. M. Zheng, H. X. Chen, J. M. Wang, K. He, B. L. Wang, T. Zhu, X. C. Zeng, M. L. Liu and M. S. Wang, *ACS Nano*, 2018, **12**, 12597–12611.

22 Y. Guo, Y. G. Zhang, Y. G. Wang, D. Y. Zhang, Y. Lu, R. J. Luo, Y. B. Wang, X. M. Liu, J. K. Kim and Y. S. Luo, *Electrochim. Acta*, 2019, **296**, 989–998.

23 N. T. Wu, X. G. Qiao, J. K. Shen, G. L. Liu, T. Sun, H. Wu, H. S. Hou, X. M. Liu, Y. Zhang and X. B. Ji, *Electrochim. Acta*, 2019, **299**, 540–548.

24 D. Zhao, J. W. Qin, L. R. Zheng and M. H. Cao, *Chem. Mater.*, 2016, **28**, 4180–4190.

25 Z. Q. Cao, M. L. Qin, B. R. Jia, L. Zhang, Q. Wan, M. S. Wang, A. A. Volinsky and X. H. Qu, *Electrochim. Acta*, 2014, **139**, 76–81.

26 B. K. Guo, M. F. Chi, X. G. Sun and S. Dai, *J. Power Sources*, 2012, **205**, 495–499.

27 Y. Zhao, J. J. Wang, C. L. Ma and Y. Li, *Chem. Phys. Lett.*, 2018, **704**, 31–36.

28 Z. Q. Cao and C. Y. Zuo, *RSC Adv.*, 2017, **7**, 40243–40248.

29 L. Y. Jiang, S. Xin, X. L. Wu, H. Li, Y. G. Guo and L. J. Wan, *J. Mater. Chem.*, 2010, **20**, 7565–7569.

30 S. M. Abbas, N. Ahmad, A. U. Rehman, U. A. Rana, S. U. D. Khan, S. Hussain and K. W. Nam, *Electrochim. Acta*, 2016, **212**, 260–269.

31 Y. Fu, H. B. Gu, X. R. Yan, J. R. Liu, Y. R. Wang, J. N. Huang, X. Y. Li, H. L. Lv, X. Z. Wang, J. Guo, G. X. Lu, S. Qiu and Z. H. Guo, *Chem. Eng. J.*, 2015, **277**, 186–193.

32 S. H. Liu, Z. Y. Wang, C. Yu, H. B. Wu, G. Wang, Q. Dong, J. S. Qiu, A. Eychmuller and X. W. Lou, *Adv. Mater.*, 2013, **25**, 3462–3467.

33 Z. Y. Lin, G. Z. Liu, Y. P. Zheng, Y. B. Lin and Z. G. Huang, *J. Mater. Chem. A*, 2018, **6**, 22655–22661.

34 S. J. Hao, B. W. Zhang, Y. Wang, C. J. Li, J. Y. Feng, S. Ball, M. Srinivasan, J. S. Wu and Y. Z. Huang, *Electrochim. Acta*, 2018, **260**, 965–973.

35 W. Q. Cao, W. Z. Wang, H. L. Shi, J. Wang, M. S. Cao, Y. J. Liang and M. Zhu, *Nano Res.*, 2018, **11**, 1437–1446.

36 J. P. Perdew, K. Burke and M. Ernzerhof, *Phys. Rev. Lett.*, 1996, **77**, 3865–3868.

37 P. E. Blöchl, *Phys. Rev. B*, 1994, **50**, 17953–17979.

38 P. E. Blöchl, O. Jepsen and O. K. Andersen, *Phys. Rev. B*, 1994, **49**, 16223–16233.

39 G. Stefan, *J. Comput. Chem.*, 2006, **27**, 1787–1799.

40 N. T. Wu, J. K. Shen, L. Sun, M. Y. Yuan, Y. Y. Shao, J. M. Ma, G. L. Liu, D. L. Guo, X. M. Liu and Y. B. He, *Electrochim. Acta*, 2019, **310**, 70–77.

41 Z. Q. Zhu, Y. X. Tang, Z. S. Lv, J. Q. Wei, Y. Y. Zhang, R. H. Wang, W. Zhang, H. R. Xia, M. Z. Ge and X. D. Chen, *Angew. Chem., Int. Ed.*, 2018, **57**, 3656–3660.

42 K. N. Zhao, F. N. Liu, C. J. Niu, W. W. Xu, Y. F. Dong, L. Zhang, S. M. Xie, M. Y. Yan, Q. L. Wei, D. Y. Zhao and L. Q. Mai, *Adv. Sci.*, 2015, **2**, 4443–4464.

43 M. Zhang, Y. W. Li, E. Uchaker, S. Candelaria, L. F. Shen, T. H. Wang and G. Z. Cao, *Nano Energy*, 2013, **2**, 769–778.

44 J. Sun, H. W. Lee, M. Pasta, Y. M. Sun, W. Liu, Y. B. Li, H. R. Lee, N. Liu and Y. Cui, *Energy Storage Materials*, 2016, **4**, 130–136.

45 J. Cui, S. Yao, J. Q. Huang, L. Qin, W. G. Chong, Z. Sadighi, J. Huang, Z. Wang and J. K. Kim, *Energy Storage Materials*, 2017, **9**, 85–95.

46 J. Hu, H. Li and X. J. Huang, *Electrochem. Solid-State Lett.*, 2005, **8**, A66–A69.

47 Y. Zhao, J. J. Wang, C. L. Ma and Y. Li, *Chem. Phys. Lett.*, 2018, **704**, 31–36.

48 H. Xu, M. Zeng and J. Li, *Int. J. Electrochem. Sci.*, 2015, **10**, 7361–7370.

49 S. Ma, Y. M. Xu, X. L. Cheng, X. F. Zhang, S. Gao, H. Zhao and L. H. Huo, *Int. J. Electrochem. Sci.*, 2018, **13**, 6048–6058.

50 G. Zhao, T. Wen, J. Zhang, J. Li, H. Dong, X. Wang, Y. Guo and W. Hu, *J. Mater. Chem. A*, 2014, **2**, 944–948.

51 H. Liu, X. W. Du, X. R. Xing, G. X. Wang and S. Z. Qiao, *Chem. Commun.*, 2012, **48**, 865–867.

52 T. Yang, Z. Chen, H. Zhang, M. Zhang and T. Wang, *Electrochim. Acta*, 2016, **217**, 55–61.

53 Y. Xiang, Z. Chen, C. M. Chen, T. H. Wang and M. Zhang, *J. Alloys Compd.*, 2017, **724**, 406–412.

54 X. Zhao, Q. C. Zhuang, S. D. Xu, Y. X. Xu, Y. L. Shi and X. X. Zhang, *J. Electrochem. Soc.*, 2015, **162**, A1156–A1162.

55 F. Wang, W. Li, M. Y. Hou, C. Li, Y. G. Wang and Y. Y. Xia, *J. Mater. Chem. A*, 2015, **3**, 1703–1708.

56 T. Brezesinski, J. Wang, S. H. Tolbert and B. Dunn, *Nat. Mater.*, 2010, **9**, 146–151.

57 C. Yang, Y. L. Zhang, F. Lv, C. F. Lin, Y. Liu, K. Wang, J. R. Feng, X. H. Wang, Y. J. Chen, J. B. Li and S. J. Guo, *J. Mater. Chem. A*, 2017, **5**, 22297–22304.

58 J. Cui, S. Yao, Z. H. Lu, J. Q. Huang, W. G. Chong, F. Ciucci and J. K. Kim, *Adv. Energy Mater.*, 2018, **8**, 1702488.

59 S. Yao, J. Cui, Y. Deng, W. G. Chong, J. Wu, M. Ihsan-Ul-Haq, Y. W. Mai and J. K. Kim, *Energy Storage Materials*, 2019, **20**, 36–45.

60 C. T. Zhao, C. Yu, M. D. Zhang, H. W. Huang, S. F. Li, X. T. Han, Z. B. Liu, J. Yang, W. Xiao, J. N. Liang, X. L. Sun and J. S. Qiu, *Adv. Energy Mater.*, 2017, 1602880.

61 J. Hassoun, F. Bonaccorso, M. Agostini, M. Angelucci, M. G. Betti, R. Cingolani, M. Gemmi, C. Mariani, S. Panero, V. Pellegrini and B. Scrosati, *Nano Lett.*, 2014, **14**, 4901–4906.

62 Z. G. Yin, J. W. Qin, W. Wang and M. H. Cao, *Nano Energy*, 2017, **31**, 367–376.